

# Plasmonics on a Neural Implant: Engineering Light–Matter Interactions on the Nonplanar Surface of Tapered Optical Fibers

Filippo Pisano,\* Muhammad Fayyaz Kashif, Antonio Balena, Marco Pisanello, Francesco De Angelis, Liset M de la Prida, Manuel Valiente, Antonella D’Orazio, Massimo De Vittorio, Marco Grande, and Ferruccio Pisanello\*

Optical methods are driving a revolution in neuroscience. Ignited by optogenetic techniques, a set of strategies has emerged to control and monitor neural activity in deep brain regions using implantable photonic probes. A yet unexplored technological leap is exploiting nanoscale light-matter interactions for enhanced bio-sensing, beam-manipulation and opto-thermal heat delivery in the brain. To bridge this gap, we got inspired by the brain cells’ scale to propose a nano-patterned tapered-fiber neural implant featuring highly-curved plasmonic structures (30  $\mu\text{m}$  radius of curvature, sub-50 nm gaps). We describe the nanofabrication process of the probes and characterize their optical properties. We suggest a theoretical framework using the interaction between the guided modes and plasmonic structures to engineer the electric field enhancement at arbitrary depths along the implant, in the visible/near-infrared range. We show that our probes can control the spectral and angular patterns of optical transmission, enhancing the angular emission and collection range beyond the reach of existing optical neural interfaces. Finally, we evaluate the application as fluorescence and Raman probes, with wave-vector selectivity, for multimodal neural applications. We believe our work represents a first step towards a new class of versatile nano-optical neural implants for brain research in health and disease.


## 1. Introduction

The fields of photonics and neuroscience are enjoying a virtuous circle, where breakthroughs in one field spur novel research endeavors in the other. In particular, the rise of optogenetic techniques in neurobiology ignited the growth of a vibrant neurophotonic community<sup>[1]</sup> that, in turn, developed a technological platform centered on radiative optoelectronic interfaces to stimulate and monitor neural activity. These interfaces include photonic probes integrated with waveguides, micro-LEDs (light-emitting diodes), and recording electrodes alongside implantable, multifunctional optical fibers.<sup>[2,3–15]</sup>

After a decade of continuous innovation,<sup>[16]</sup> there is growing agreement that next-generation probes should provide access to neural dynamics in the electrical, optical, biochemical, and mechanical domains.<sup>[17]</sup> Recently, the field started to explore optically confined systems at

F. Pisano, A. Balena, M. Pisanello, M. De Vittorio, F. Pisanello  
Istituto Italiano di Tecnologia  
Center for Biomolecular Nanotechnologies  
Arnesano (LE) 73010, Italy  
E-mail: filippo.pisano@iit.it; ferruccio.pisanello@iit.it  
M. F. Kashif, A. D’Orazio, M. Grande  
Dipartimento di Ingegneria Elettrica e dell’Informazione  
Politecnico di Bari  
Bari 70125, Italy

F. De Angelis  
Istituto Italiano di Tecnologia  
Plasmon Nanotechnologies  
Genova 16163, Italy  
L. M. de la Prida  
Instituto Cajal  
CSIC  
Madrid 28002, Spain  
M. Valiente  
Brain Metastasis Group  
CNIO  
Madrid 28029, Spain  
M. De Vittorio  
Dipartimento di Ingegneria dell’Innovazione  
Università del Salento  
Lecce 73100, Italy

 The ORCID identification number(s) for the author(s) of this article can be found under <https://doi.org/10.1002/adom.202101649>.

© 2021 The Authors. Advanced Optical Materials published by Wiley-VCH GmbH. This is an open access article under the terms of the Creative Commons Attribution-NonCommercial License, which permits use, distribution and reproduction in any medium, provided the original work is properly cited and is not used for commercial purposes.

DOI: 10.1002/adom.202101649

the sub-micrometer scale, aiming to establish new paradigms based on light–matter interactions<sup>[18–28]</sup>

Harnessing light–matter interactions at the nanoscale on a neural probe would pave the way toward enhanced biomolecular sensing, for example, surface enhanced Raman scattering (SERS), refractive index sensing, metal-enhanced fluorescence, and highly localized and ultrafast heat delivery. At the same time, the modulation of the radiative field through sub-wavelength structures has the potential to open new perspectives for light delivery and collection in scattering tissue, for example, through extraordinary optical transmission (EOT)<sup>[29,30]</sup> or plasmonic beaming.<sup>[31,32]</sup>

Yet, neuroplasmonic technologies are still at their embryonal stage, and the community currently lacks methods to incorporate plasmonic structures on implantable optical neural interfaces. To bridge this gap, we developed an all-optical implantable plasmonic probe based on low-invasive nanostructured tapered optical fibers (nTFs) to obtain controlled field enhancement in arbitrarily deep brain regions, where the photonic approach is sometimes hindered by intrinsically weak signals. nTFs exploit the effect of the narrowing waveguide on the transversal component of the wavevector of guided modes to excite a curved plasmonic structure milled on the highly nonplanar surface of the fiber taper. With theoretical modeling support, we show that the field enhancement on the nTFs can be modulated in the visible and near-infrared ranges acting on plasmonic structures with footprints comparable to the dimension of brain cells.

Notably, the photonic properties of the nTFs shape the emission and the collection geometry of the probe to enable new classes of biological applications. The combination of EOT effects with the mode-selective light-collection properties of nTFs allows for selective collection of highly directional, 25  $\mu\text{m}$  wide beamlets that can be tuned within a 120° span (−70°, +50°) around the fiber. Accordingly, specific Raman bands can be excited and collected through EOT at arbitrary confined position along the fiber. These results make us envision that nTFs represent a promising strategy to explore versatile nano-optical neural interfaces in vivo.

## 2. Results

### 2.1. Plasmonic Structures on the Curved Taper Edge

Neurons and other brain cells of 10–30  $\mu\text{m}$  size are typically scattered or arranged in spatially defined layouts. Thus, we realized a plasmonic neural probe by milling metallic nanopatterns on a multimode tapered optical fiber using comparable dimensions (Figure 1a). As a peculiar feature, the narrowing waveguide directly acts on the transversal component  $k_t$  of the guided wavevector,<sup>[33,34]</sup> enabling the combination of the superficial component of the wavevector  $k_s$  with the reciprocal lattice vector of the nanopattern (Figure 1b). In the case of a curved nanograting (cNG), slits arranged perpendicularly to the fiber axis couple with the superficial tangential component of the guided wavevector and generate a surface plasmon resonance (SPR) following

$$\vec{k}_{\text{SPR}} = \vec{k}_s + i\vec{G}_s \quad (1)$$

where  $\vec{k}_{\text{SPR}}$  is the surface plasmon wavevector,  $\vec{k}_s$  is the component on the taper surface of the light guided into the fiber, and  $|\vec{G}_s| = \frac{2\pi}{p}$  is the reciprocal lattice vector for the nanograting with period  $p$ .<sup>[35]</sup> While condition (1) is a first approximation that does not consider the fiber curvature, it clarifies that the spectral position of the resonance depends on the curved nanograting periodicity.

To fabricate the nanostructures, the taper was coated with a conformal coating of gold to establish a metal-confined optical waveguide (Au thickness = 100–150 nm, 5 nm of Cr as adhesion layer, see Materials and Methods). To ensure a uniform gold coating, the fiber surface was homogeneously exposed to a directional electron beam evaporation using a rotating motor. To ease future testing of different geometries for neural applications, we patterned different arrays of plasmonic structures along the taper using focused ion beam (FIB) milling. Figure 1c shows a curved nanograting imaged with a scanning electron microscope (SEM), while Figure 1d displays SEM close-ups of the curved arrays to highlight nanoplatelets and nanoholes, as well as the crossing lines at high milling resolution. Milling at low currents (7.7 pA) and small Ga<sup>+</sup> beam diameters (9.8 nm)<sup>[36]</sup> enabled the realization of sub-50 nm features on the curved fiber surface (Figure 1d). The repeatability of the fabrication process ensured a homogeneous onset of plasmonic resonances on multiple structures milled on the same fiber, as demonstrated by the dark field image of four neighboring cNGs (Figure 1e).

### 2.2. Optical Characterization of Surface Plasmon Resonances on the Taper Surface

To characterize the optical response of nTFs, we measured the dispersion diagrams of a curved nanograting as a function of the grating periodicity  $p$  using Fourier microspectroscopy (Figure 2a). To this purpose, the nTF got excited with incoherent broadband light from a butt-coupled fiber patch cord. The curved nanograting was set at the center of the field of view in the focal plane of a high numerical aperture (NA) objective (50 $\times$ , NA = 0.75), with the fiber axis being perpendicular to the objective axis and emitted light modulated by the SPR. To image this modulation, the back-focal plane (BFP) of the objective was relayed on the slits of a spectrometer (Horiba, iHR320) using a Bertrand lens positioned behind the objective ( $f = 100$  mm) and a tube lens ( $f = 200$  mm).<sup>[37]</sup> The polarization of the emitted light was discriminated with a linear polarizer. Then, the fiber and the objective were progressively displaced under the Bertrand lens in order to image the full angular acceptance of the objective on the thin spectrometer's charge-coupled device (CCD) camera. Finally, we reconstructed the dispersion diagram by stitching the images of emission across the full angular acceptance of the objective. Dispersion diagrams for cNGs with a radius of curvature,  $r = 30$   $\mu\text{m}$ ; longitudinal side,  $T = 25$   $\mu\text{m}$ ; and arc length,  $L = 24$   $\mu\text{m}$ ; slit width  $w = 100$  nm, and periodicity  $p = 630, 700,$  and  $750$  nm are shown in Figure 2b. These diagrams illustrate the complex resonant patterns that arise from the combination of modal propagation in the tapered fibers with the plasmonic modes on the curved nanograting. In Figure S1a (Supporting Information),

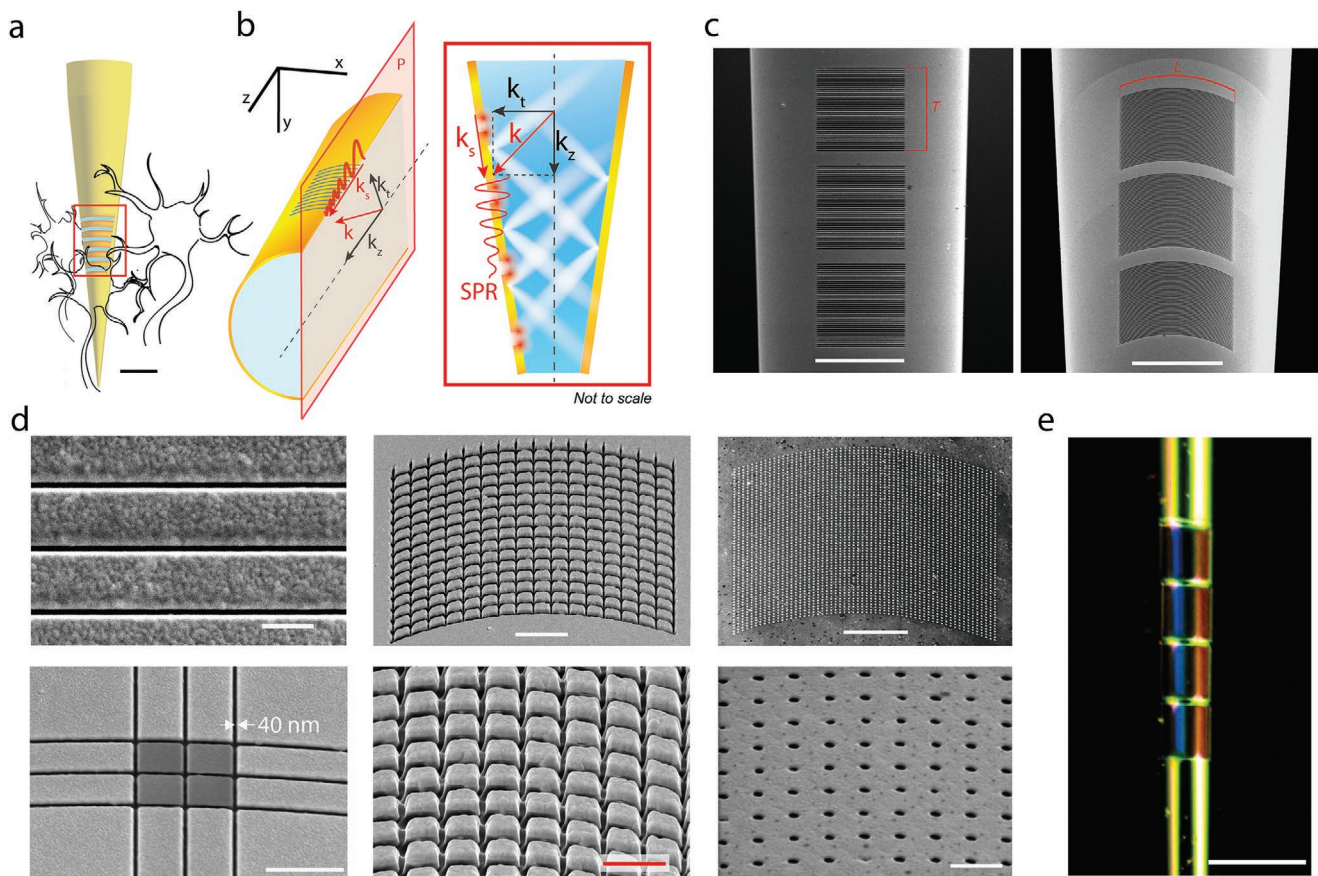


**Figure 1.** Plasmonic structures on the curved surface of nTF designed for neural applications. a) Conceptual diagram of a neural implant based on a metal-coated tapered fiber hosting a plasmonic nanostructure with footprint comparable to the soma of a single neuron (the scale bar is 25  $\mu\text{m}$ ). b) 3D and side views of the excitation mechanism of surface plasmon resonances; when broadband light guided in the taper illuminates the nanograting, the superficial component  $k_s$  of the guided light couples with the grating periodicity. If the momentum matching condition in Equation (1) is satisfied, an SPR is generated at the dielectric-metal interface. b-left) A 3D view where a plane  $P$  passing through the waveguide axis and the nanograting center is used to define a representation of the guided wavevectors; the scale bars represent 25  $\mu\text{m}$  in the three spatial directions. b-right) A simplified view of the effect, not to scale. c) SEM images of curved nanogratings (cNG) milled on Au-coated tapered optical fibers: (left) top view, (right) tilted view. The scale bars are 25  $\mu\text{m}$ . Note that such a layout allows potential recording of signals from different cells. d) Close-ups of different nanostructures milled on the fiber; (left) minimum feature size of 40 nm for a curved (top) and crossing curved lines on the taper surface; top left and bottom left scale bars are 1  $\mu\text{m}$ . Middle: a 2D curved array of nanoplatelets (top) and a zoom on the nanoplatelets (bottom); top middle and bottom middle scale bars are 1  $\mu\text{m}$ . Right: a curved array of nanoholes (top, inverted grayscale) and a close up on 100 nm diameter nanoholes on the fiber's surface; top right scale bar is 2  $\mu\text{m}$ , bottom right scale bar is 2  $\mu\text{m}$ . e) A dark field image of four curved nanograting with  $p = 600$  nm milled on the same tapered fiber.

the predicted energy dispersion SPR and the loci of Wood's anomalies (WA) are superimposed to the diagrams according to the following equations (Equations (2) and (3)), respectively, calculated at the silica–gold and gold–air interface<sup>[35,38]</sup>

$$|\vec{k}_{\text{SPR}}| = \frac{\omega}{c} \sqrt{\frac{\epsilon_d \cdot \epsilon_m}{\epsilon_d + \epsilon_m}} \quad (2)$$

$$|\vec{k}_w| = \frac{\omega}{c} \sqrt{\epsilon_d} \quad (3)$$

where  $\omega$  is the frequency,  $\epsilon_d$  is the dielectric constant of silica or air,  $\epsilon_m$  is the dielectric constant of gold, and  $\vec{k}_w$  is the wavevector of grazing light that originates the Wood's anomaly. The data shown in Figure 2b are reported also for transverse electric (TE) polarizations in Section S1 and Figure S1b (Supporting Information).

As expected, we observed that resonances shifted according to the grating periodicity. Interestingly, we detected light emitted from the curved nanograting toward the larger part of the taper cone, pointing away from the taper tip. This is a peculiar feature with respect to previous observations of light emission from smooth optical apertures of metal-coated tapered optical fibers.<sup>[39,40]</sup> It arises from the interaction between both forward- and backpropagating light with the grating, i.e., introduced by light confined by the metal layer and back-reflected at the taper tip,<sup>[41]</sup> as testified by the signs of the impinging wavevector and the vectorial momentum matching relation (1) (see Section S2 in the Supporting Information). The spectral positions of maxima and minima of transmissions were consistent across experiments and simulations, obtained by rigorous coupled wave analysis (RCWA) for a planar grating (see Section S3 and Figures S2–S6, Supporting Information). At the same time, the moderate deviations of the measured resonances with respect

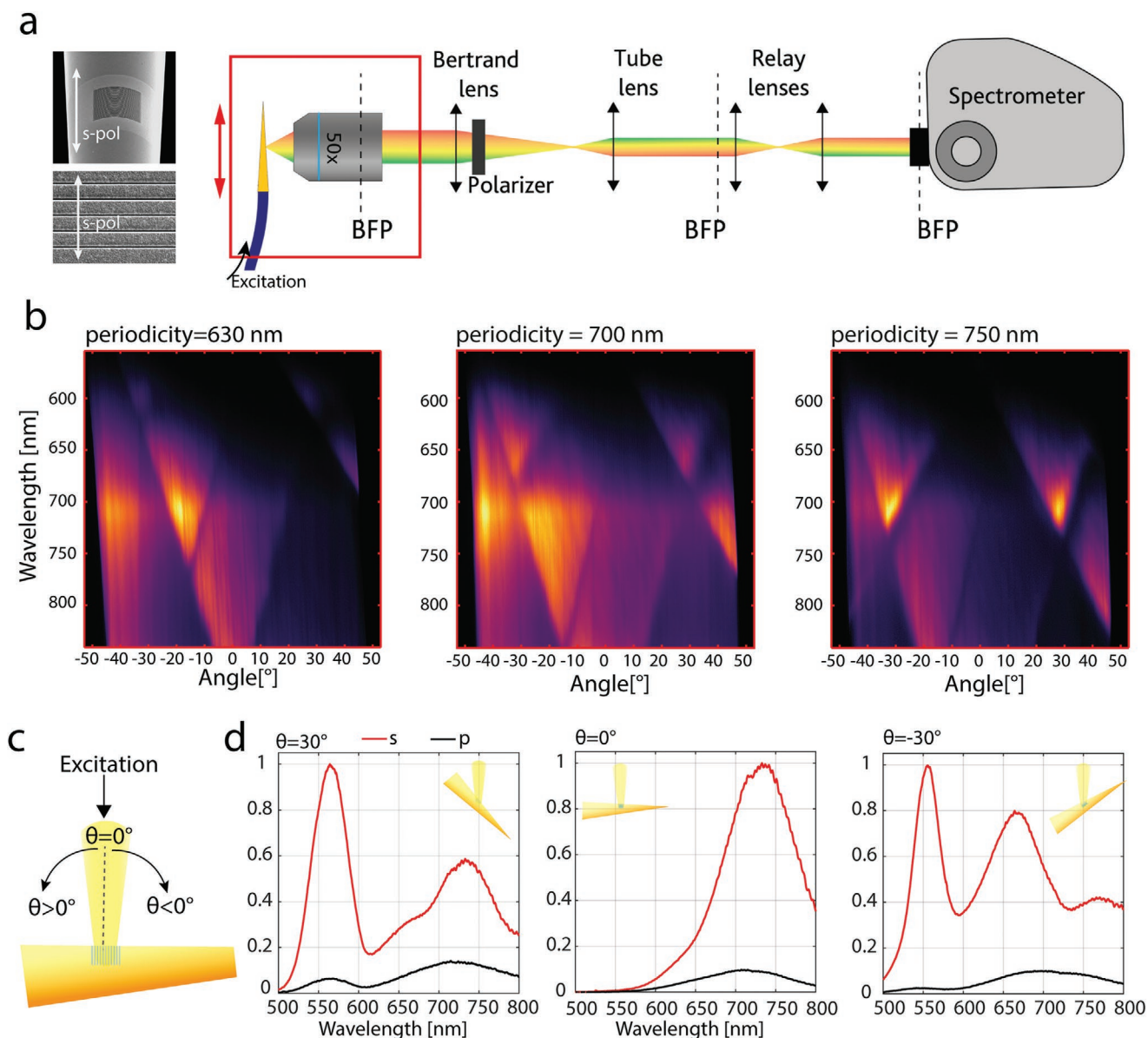


**Figure 2.** Spectrally tunable surface plasmon resonances on the curved fiber surface. a) Diagram of the Fourier microscopy system used to measure the dispersion diagrams for curved nanograting at several periodicities. Incoherent light is launched in the tapered fiber and gets emitted from the cNG. The Fourier plane of the emission is imaged on a spectrometer, displacing the fiber-objective system to cover the full angular collection range. b) Dispersion diagrams for curved nanograting milled with periodicity of (left) 630 nm, (center) 700 nm, and (right) 750 nm. c) Schematic of the optical arrangement for the transmission measurements. The nTF with a curved nanograting is progressively tilted under a low-NA objective while a loosely focused spot impinges on the grating. The transmitted light is collected through the fiber. d) EOT through the curved nanograting at periodicity  $p = 630$  nm for light impinging at  $-30^\circ$  (left, tip pointing down),  $0^\circ$  (center), and  $30^\circ$  (right, tip pointing upward). The spectra for s- and p-polarized illumination are shown in red and black lines, respectively.

to the expected positions were consistent with the simulations; so, we attribute them to discrepancies in the actual and modeled refractive indices.

To corroborate the description of SPR on the taper edge, we measured the collection spectrum of light collected by the curved nanograting when illuminated at near-normal incidence from the air side. To do this, we positioned the fiber at an angle under a low-NA objective ( $5\times$ ,  $\text{NA} = 0.16$ ) and we illuminated the curved nanograting with a spot of linearly polarized, incoherent broadband light, with the electric field being perpendicular

to the grating slits (s-polarization) (Figure 2c). To obtain a spot matching the curved nanograting size, the illumination was spatially filtered with a pinhole, whose image was then relayed on the curved nanograting (see Experimental Section). The collection spectra for s-polarized light indicated a strong spectral modulation that depends on the impinging angle, while p-polarized light did not (Figure 2d). A residual modulation on the p-polarization can be explained with an imperfect alignment of the polarizer. As expected from the dispersion diagrams in emission (Figure 2b), we observed collection

of light impinging on the nanograting at positive angles (Figure 2c) and found an overall consistency of the spectral features observed in the two experimental configurations (Figure S8, Supporting Information), such as the more efficient collection of light that impinges on the nanograting at a negative angle (Figure 2c; Figure S9, Supporting Information). Also in this case, this behavior was not present when light is collected with smooth optical apertures in metal-coated tapered fibers.<sup>[39,40,42]</sup> The asymmetry in the spectra acquired at  $+30^\circ$  and  $-30^\circ$  can be attributed to the nontrivial combination of EOT on the nanogratings with the mode-dependent light collection properties of tapered optical fibers (see Section S5 in the Supporting Information). The results summarized in Figure 2 demonstrate that it is possible to excite SPR on tapered fibers' neural implants and that the spectral behavior can be tuned acting on simple geometrical parameters such as the grating periodicity.

### 2.3. Wavevector-Encoded Fluorescence Collection

As shown above, nTFs can be tuned to work at a desired spectral range. Intriguingly, the combination of wavevector selectivity of curved nanograting with the mode-selective collection properties of tapered optical fibers<sup>[42]</sup> can be exploited to impose a spectral modulation on narrow angular ranges of light emitted or collected by the probe depending on its spectral content. Such distinctive features of curved nanogratings could ease unique biological applications of nTFs.

To assess this, we fabricated an nTF with a curved nanograting tuned to collect visible fluorescence light in a homogeneous fluorescent solution (RI = 1.33) ( $p = 475$  nm,  $w = 100$  nm, and  $h = 130$  nm). We built a collection map of the curved nanograting using a two-photon scanning system to generate fluorescent point-like spots near the nanostructured fibers immersed in a homogeneous fluorescent solution (Figure 3a).<sup>[39,40,42]</sup> Then, we used a second detector at the fiber output, synchronized with the scanning beam, to detect the fluorescence collected by the grating. This generated a high-resolution collection diagram covering the  $-90^\circ:90^\circ$  angular range around the normal to the curved surface. To measure the dependence of the collection diagram on the impinging wavelengths, we alternatively placed fluorescence filters in the collection path to discriminate the contribution of neighboring spectral ranges (Figure 3a).

We found that the EOT properties of the cNG, combined with the modal selectivity of the fiber, generated a collection diagram with three well-distinct, directional beamlets, labeled as  $\alpha$ ,  $\beta$ , and  $\gamma$  in Figure 3b,c. As expected, the angular direction of the beamlets depended on the spectral content of the transmitted light (Table 1). Figure 3b shows the collection diagram for fluorescence at 510–560 nm, while Figure 3c shows the case for 570–640 nm. The collection diagram of the curved nanograting was markedly different from that of a smooth optical window in a metal-coated fiber, which exhibited a single lobe oriented toward the fiber tip (Figure 3d). These three quasicollimated beamlets of the curved nanograting collection, instead, rotate according to the incidence wavelength. As the

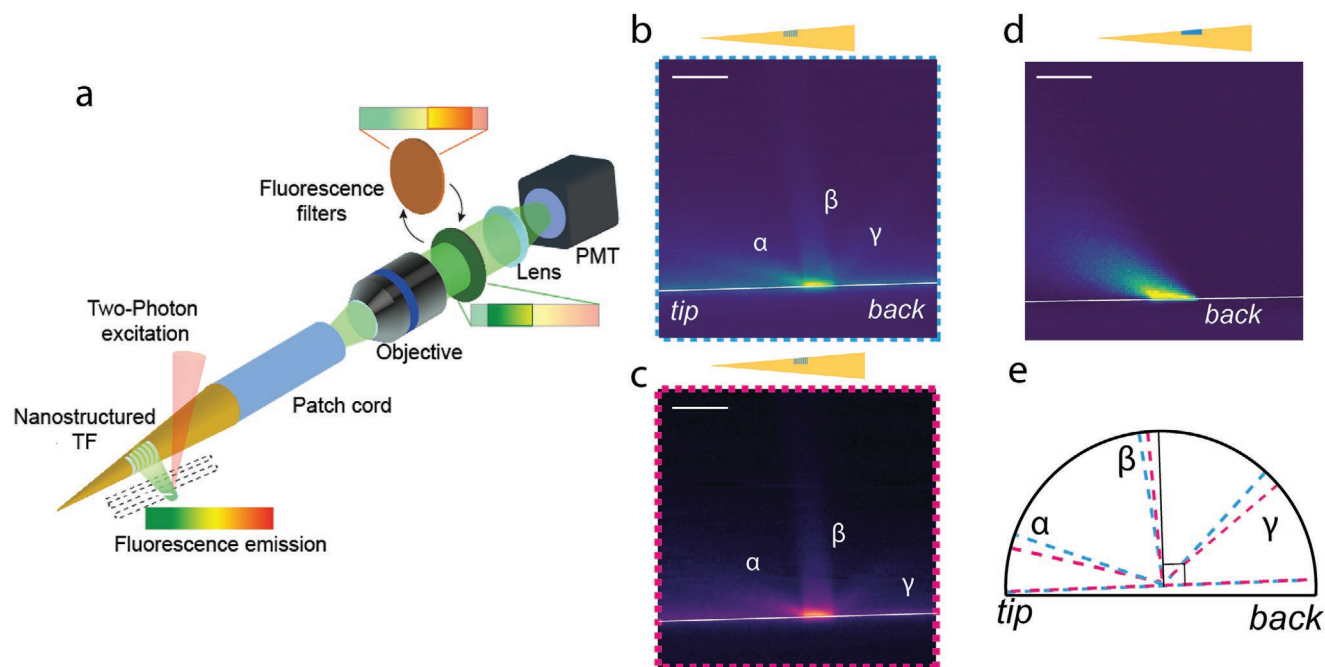


**Figure 3.** Wavevector-encoded light collection. a) Diagram of the two-photon scanning system used to characterize the collection diagram for cNGs. A two-photon spot is scanned next to the curved nanograting when the fiber is immersed in a fluorescent solution. The fluorescence collected by the curved nanograting is transmitted by the fiber and filtered with two alternative fluorescence filters before reaching the detection PMT. b) Collection diagram for fluorescent light in the range of 510–560 nm. The three collection lobes are labeled as i), ii), and iii). The white line is the fiber surface. c) As in panel (b) for 570–640 nm light. d) Collection for a smooth optical window milled on a metal-coated tapered fiber. Scale bar is 50  $\mu\text{m}$ . e) Summary of the preliminary directions of collections observed in the 510–560 (cyan) and 570–640 (magenta) channels.

**Table 1.** Direction of the collection lobes with respect of the normal to the taper surface. Positive angles are inclined toward the fiber tip.

	$\alpha$	$\beta$	$\gamma$
Green filter (510–560 nm)	69°	7°	–35°
Red filter (570–640 nm)	84°	3°	–51°

collected wavelength increases, beamlets  $\alpha$  and  $\gamma$  increase their angle with respect to the normal to the fiber surface, while beamlet  $\beta$  closes in on the normal (Figure 3e). We attribute this effect to the combination of multiple orders in the momentum matching that underlies the curved nanograting EOT (see Section S5 and Figures S7 and S10 in the Supporting Information).

These results suggest that the nTFs can collect light (and reciprocally emit) from tunable, highly directional beamlets across an enhanced angle of  $\approx 120^\circ$ . Potentially, this will enable establishing a link between the direction and the spectral content of fluorescence light collected through a fiber implant, a feature that is beyond the reach of existing optical neural interfaces.

#### 2.4. Engineering the Field Enhancement on the nTFs for Plasmon-Assisted Raman Spectroscopy

Next, we evaluated whether nTFs allow engineering both field enhancement and optical transmission at multiple wavelengths. This capability is particularly relevant for label-free biochemical sensing applications, such as Raman spectroscopy, where the excitation wavelength and the scattered signal have a significant spectral separation. To do this, we focused on the detection of Raman signal in the lipid bands, a ubiquitous spectral signature in biological samples, which has recently been shown to play a pivotal role in discriminating healthy from cancerous tissue during surgical procedures.<sup>[43]</sup> As a convenient phantom to mimic the Raman response of brain lipid bands, in both the fingerprint and the high-wavenumber region, we used olive oil. This is because olive oil shares many lipid signatures with biological tissue<sup>[44,45]</sup> (for example strong peaks at 1441  $\text{cm}^{-1}$  and in the 2800–3000  $\text{cm}^{-1}$  regions), and its optical properties are well known (e.g., refractive index and third-order nonlinearities). We therefore used a 3D finite-difference time-domain (FDTD) model to simulate the electric field on the curved nanograting for an excitation wavelength of 785 nm and a scattered signal of 885 nm (1441  $\text{cm}^{-1}$ ) and 1015 nm (2887  $\text{cm}^{-1}$ )<sup>[46]</sup> (see the Experimental Section). As detailed in Section S6 (Supporting Information), and Figure S11 (Supporting Information), we modeled the excitation electric field as a plane wave impinging at  $\vartheta = 60^\circ$  on the nanograting.

To ensure a relevant field enhancement while maximizing optical transmission, we used a curved nanograting with periodicity  $p = 600$  nm, gap size  $w = 470$  nm, height  $h = 130$  nm, arc length  $l = 24$   $\mu\text{m}$ , and radius of curvature  $r = 30$   $\mu\text{m}$ . Figure 4 shows the squared intensity of the electric field components on the curved nanograting slits. The field enhancement is shown as a color bar next to every panel. In particular, Figure 4a displays the cross section of the curved nanograting slit when receiving 785 nm illumination at  $60^\circ$ , while Figure 4b,c focuses

on the center of the slit and on the corner of the slit. Similarly, Figure 4d–f is dedicated to the field enhancement for 885 nm light impinging on the curved nanograting from the surrounding medium. Lastly, Figure 4g–i shows the magnitude of the field when 1015 nm light illuminates the grating from outside the waveguide. We observed that the predominant field enhancement was located at the silica–gold interface for all these three wavelengths. Hotspots on the top edge of the slit edges arose at the center of the slit for 785 nm (Figure 4b) and on the corner of the slit for 1015 nm (2887  $\text{cm}^{-1}$ ). In addition, there was a sizeable field enhancement (8–10) in the dielectric area for 785 nm (Figure 4a) and 885 nm (1441  $\text{cm}^{-1}$ , Figure 4e).

#### 2.5. Plasmon-Assisted Raman Endoscopy

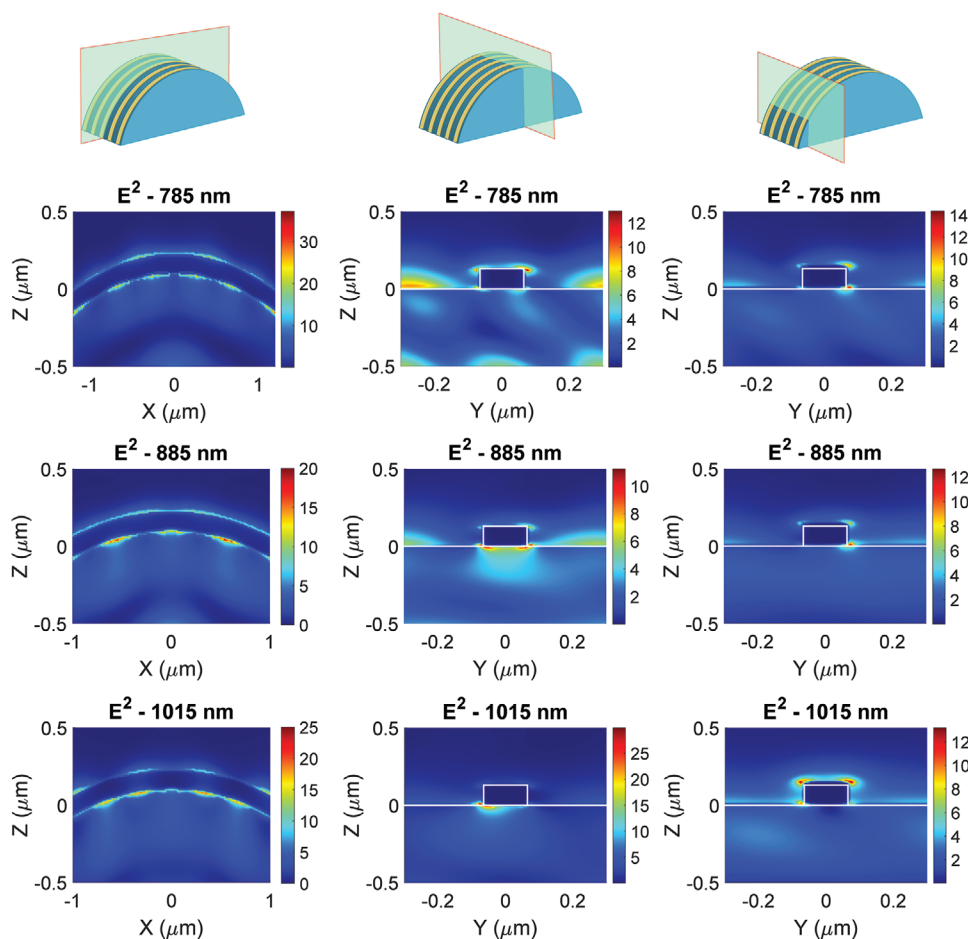
Encouraged by the strength of the numerical model described above, we investigated the possibility of exploiting the field enhancement to employ the nTF as enhanced Raman endoscopes. To do so, we fabricated nTFs with four cNGs following the parameters described in the previous paragraph. Then, we immersed the nTFs in a bath of the olive oil phantom, and we injected 785 nm light from the back-facet of the fiber. To do this, we held the probe with a 5 axis manipulator in the focal spot of a custom confocal Raman microscope, with the polished back-end facing the objective (Figure 5a; see the Experimental Section). The 785 nm excitation, released through the curved nanograting via EOT, generated a Raman signal that was collected through the same curved nanograting and propagated in the fiber toward the objective. The Raman signal was discriminated from the 785 nm pump using a dichroic mirror and long-pass filter before being detected with a spectrometer (Horiba, iHR320).

Figure 5b,c shows the Raman signal of the lipid bands of olive oil at 1441  $\text{cm}^{-1}$  (Figure 5b) and 2887  $\text{cm}^{-1}$  (Figure 5c). For comparison, the Raman signal collected through the nTFs is plotted against a reference Raman spectrum acquired with an objective and normalized to the nTF signal. Using  $\approx 50$  mW of illuminating power, corresponding to 40  $\mu\text{W}$  emitted by the patterned area, we detected 3 counts  $\text{s}^{-1}$  on the Raman peaks after subtracting the silica background (Figure 5b).

To determine if the signal we measured arose from volumetric Raman signal or from surface-enhanced Raman, we simulated the intensity of lipidic Raman bands excited and collected through the curved nanograting from a thin layer of olive oil (0.5  $\mu\text{m}$ ) encapsulating the fiber (Figure 5c) while tuning the nonlinear optical response using an FDTD method (see the Experimental Section). The oil was modeled through dispersive third-order nonlinear properties  $\chi^3$  using a Lorentz-like oscillator for a given resonance with

$$\chi^3(\omega) = \alpha\chi_0^3 + (1 - \alpha) \frac{\chi_0^3 \omega_{\text{RAMAN}}}{\omega_{\text{RAMAN}}^2 - 2j\delta\omega - \omega^2} \quad (4)$$

In Equation (4) the  $\alpha$  parameter splits the third-order nonlinearity into a Kerr and Raman effect, and sets the relative strength of each interaction,  $\omega_{\text{RAMAN}}$  is the Raman resonance frequency,  $\chi_0^3$  is the third-order electric susceptibility of the oil,<sup>[47]</sup> and  $\delta$  is the damping factor, which controls the line width of the resonance



**Figure 4.** Electric field enhancement on the cNG. a) Transversal view of the electric field intensity on a cNG slit at 785 nm impinging from the silica side at 60°. b) Longitudinal view of the electric field intensity on the central portion of a cNG slit for 785 nm impinging from the silica side at 60°. c) As in panel (b) for a portion at the edge of the cNG. d–f) As in panels (a) and (b) for 885 nm light that illuminates the cNG from the surrounding medium (olive oil) at 60°. g–i) As in panels (d–f) for 1015 nm light. The colorbars beside each panel represent the field enhancement calculated as  $E^2/E_{\text{incident}}^2$ .

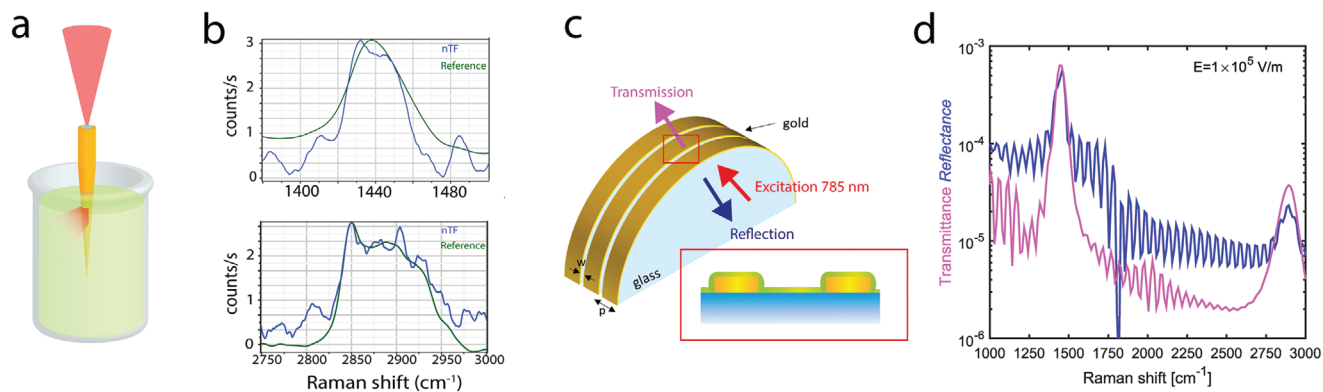


**Figure 5.** Plasmon-assisted Raman spectroscopy with nTFs. a) Sketch of the experimental measurement. The nTF, immersed in olive oil, receives illumination from the back facet. The 785 nm light is emitted from the curved nanograting that, in turn, collects the Raman signal and couples it with the waveguide. The signal emerging from the fiber is routed to a spectrometer (not shown). b) Raman spectra of olive oil collected with the nTF (blue) and with a standard objective lens (green) around the 1441  $\text{cm}^{-1}$  (top) and 2800–3000  $\text{cm}^{-1}$  (bottom) bands. The intensity counts of the reference signals have been normalized to the nTF measurements for the ease of comparison. c) Schematics of the 3D model of the cNG, with an inset detailing the presence of the analyte. d) Simulated Raman spectrum in reflection (blue) and transmittance (magenta) for an input electric field of  $1 \times 10^5 \text{ V m}^{-1}$ .

(see the Experimental Section).<sup>[48]</sup> The Raman spectra in reflection and transmission configurations for 885 nm ( $1441\text{ cm}^{-1}$ ) are shown in Figure 5d for an input electric field of  $10^5\text{ V m}^{-1}$ , the minimum pump at which a sizeable surface enhancement of the Raman signal kicks in. As shown in Section S7 and Figure S12 (Supporting Information), lower intensities do not trigger an enhancement. This implies that we cannot reach the enhancement regime as our current experimental system can deliver up to  $\approx 10^3\text{ V m}^{-1}$  on the curved nanograting through the fiber. Importantly, pumping the structures with such a high electric field would result in intensities beyond the ablation threshold of gold films,<sup>[49,50]</sup> endangering the integrity of the structures. Such an experimental limitation can be circumvented using structures with higher field enhancement; for example, gold bow-ties with nanometric gaps.<sup>[51]</sup> This would be instrumental in making spectrally specific SERS available in deep tissue regions, opening the way for label-free molecular monitoring of biochemical events, such as neurotransmitter release. Interestingly, we also noted that when a Raman signal at 885 nm ( $1441\text{ cm}^{-1}$ ) impinges on the cNG, a Raman overtone appears in the high-wavenumber region. This property can potentially be exploited in fiber-based Raman application to mirror a signal in the fingerprint region, which is strongly affected by the silica background, to the high-wavenumber region, where the silica background is practically absent.

### 3. Conclusion

We proposed an approach to incorporate nanoplasmonic structures with cellular-size footprints along a minimally invasive optical neural implant. Our work is rooted on establishing, understanding, and controlling the interplay between the photonic properties of tapered optical fibers and the nano-optical phenomena arising on periodic subwavelength metallic structures realized on the taper surface.

Our achievements are focused on the following main outcomes: i) nanopatterning the nonplanar surface of the taper at high resolution (sub-50 nm); ii) characterizing the surface plasmon resonances induced on the tapered surface when light guided in the fiber illuminates the gratings, leveraging on the effect of the taper on the transversal component of guided modes; iii) engineering the field enhancement using a numerical model of curved nanogratings; iv) demonstrating the potential exploitation of nTFs for resonant collection of fluorescence and endoscopic Raman spectroscopy using structures comparable to brain single cells ( $25\text{ }\mu\text{m} \times 25\text{ }\mu\text{m}$ ).

The resonant collection of fluorescence with directional beamlets, whose angle depends on the spectral content, is an intriguing capability, which complements recent works that used diffractive elements to fabricate implantable probes for light-sheet fluorescence imaging.<sup>[52]</sup> The plasmonic approach not only proves that this can be accomplished with a lossy material, but also allows using the zeroth order to impose or retrieve a spatial modulation, on the strength of the wavevector-dependent momentum matching.

At the same time, the versatility offered by integrated plasmonic beam forming holds promising potential for endoscopic Raman spectroscopy applications. In fact, controlling the

volume of tissue that interacts with the probe and the direction of light emission and collection across a broad angle, at an arbitrary depth, are all desirable features to investigate the biochemical or cytoarchitectonic alterations linked with physiological (i.e., brain development or aging) or pathological conditions (i.e., brain metastasis).

While we are confident that our approach can represent a first step toward next-generation plasmonic neural probes, we also outline potential improvements linked with the optical performances of the nanostructures. For example, it would be desirable to increase the field enhancement on the plasmonic structures by improving the interfacing of the fiber modes with plasmonic structures.<sup>[53]</sup> In this direction, previous works have proposed the integration of noble metal plasmonic nanoparticles on tapered fibers for SERS applications<sup>[41,54–57]</sup> (reviewed in ref. [58]). However, these structures respond as a random or quasirandom ensemble and do not offer an immediate strategy for beam forming. Alternatively, the growing interest on using nanograting resonances to launch surface plasmons on metallic tips for scanning near-field optical microscopy (SNOM)<sup>[59–62]</sup> might offer novel insights into the optimization of optical coupling of fiber modes and plasmonic structures in the multimode regime.

From the fabrication point of view, FIB milling may have relevant drawbacks. Despite being advantageous to pattern the curved surface of the taper, the ion milling prevents from obtaining sharp edges on the grating slits, resulting in a lower field enhancement.<sup>[63]</sup> While this drawback can be circumvented using structures with high enhancement factors such as bow-tie antennas,<sup>[64,65]</sup> ion implantation might diminish the optical transmission of exposed areas of glass, although this has been observed at higher fluencies.<sup>[40,66]</sup> While traditional methods such as electron beam lithography are hardly suitable to pattern the taper surface, other strategies such as two-photon polymerization lithography,<sup>[67]</sup> self-assembly,<sup>[68,69]</sup> or nanostencil lithography<sup>[70]</sup> might allow obtaining high lateral resolution and relevant field enhancement. In this direction, we will devote our future work to alternative design that can offer the same degree of tunability of cNGs while also providing for a stronger field enhancement. This would be instrumental in exploiting nonlinear light–matter interactions at moderate pumping intensities, in order to preserve the integrity of the metallic layer.

Looking at the evolution of the neurophotonic field, we believe that the combination of nanostructures with guided modes in fiber optics is optimally set to benefit from the progress in the broader optics community. This is particularly relevant when considering the increasing maturity of holographic techniques to control modal propagation in turbid media<sup>[71,72]</sup> together with the booming interest in optical metasurfaces, metamaterials, and their application to biological research,<sup>[73]</sup> also using dielectric materials.<sup>[74]</sup> We therefore envision that controlling the interplay between electromagnetic modes and resonant nanostructures will represent a novel frontier to study neural functions in deep brain regions.

### 4. Experimental Section

*Fabrication of Tapered Optical Fibers:* Tapered fibers were obtained from OptogeniX (www.optogenix.com) using fiber cords with NA = 0.22



and core/cladding size = 200/225  $\mu\text{m}$ ; NA = 0.39 and core/cladding = 200/225  $\mu\text{m}$ ; and NA = 0.66 core/cladding = 200/230  $\mu\text{m}$ . Details of the fabrication procedure were provided in previous works.<sup>[75]</sup>

**Fabrication of Curved Nanostructures on Tapered Fibers:** Tapered fibers were coated with an adhesion layer of Cr (5 nm) and a thin layer of Au (100–150 nm) using thermal or electron beam evaporation. During the evaporation, the fibers were rotated with a stepper motor to obtain a uniform coating. The curved nanostructures (Figure 1) were milled on the taper surface using a dual-beam FIB–SEM system (FEI Helios Nanolab 600i Dual Beam). The Ga<sup>+</sup> ion beam current was set to 7.7 pA with an accelerating voltage of 30 kV. The beam spot (9.8 nm in diameter) was scanned sequentially with minimal line overlap (5–10%) and 1  $\mu\text{s}$  dwell time.<sup>[36]</sup> The morphology of the nanostructures was characterized via scanning electron microscopy.

**Optical Characterization for Dispersion Diagrams:** A custom-made Fourier spectroscopy system was used to image the angular distribution of the spectral components modulated by cNGs when broadband incoherent light was injected into the fiber. The probe was set in the focal plane of a high-NA objective (50 $\times$ , 0.65 NA), with the fiber axis being perpendicular to the objective's one and the nanostructure at the center of the objective field of view (FOV). The back-focal plane of the objective was imaged on the spectrometer slits using a system composed of a Bertrand lens positioned behind the objective ( $f = 100$  mm), a tube lens ( $f = 200$  mm), and an image relay. To collect a wide angular range on the thin spectrometer's camera with high angular resolution, the fiber and the objective were progressively displaced under the imaging system. For each of these positions, the image on the full CCD of the spectrometer (Horiba iHR320, Sincerity) was recorded. Finally, the dispersion diagrams were obtained by stitching together images at all positions using Fiji.<sup>[76]</sup> To calibrate the dispersion diagram, the spatial displacement of the fiber-objective system was measured that covered the full emission of a fiber optic of known NA excited with a laser beam injected at the maximum acceptance angle.

**Optical Characterization for Collection Properties in Air:** The nanostructured area was placed in the focal point on a low-NA objective (50 $\times$ , 0.16 NA) with a 5D control on the position of the structure: the three spatial dimensions, the tilt angle with respect to the objective axis, and the rotation angle of the fiber around its axis. The orientation of the probes was aligned across experiments using an imaging camera. The low-NA objective delivered incoherent white light (500–800 nm) under a small focusing angle ( $\pm 3^\circ$ ). Transmission spectra were measured for increasing values of the tilt angle, as shown in Figure 2, by routing the fiber patch cord output to the spectrometer input.

**Collection Properties with Point-Like Fluorescent Sources:** The light collection properties of the nanostructured probes were measured using a custom-built optical system described in previous works.<sup>[42,77,78]</sup> Briefly, a two-photon microscope equipped with two detection paths was used; a standard “microscope” path with a photomultiplier tube (PMT, Hamamatsu) receiving fluorescent light from the excitation objective, and a “fiber” path, where a PMT received fluorescence light guided by the probe and the attached fiber patch. The focal spot generated by a water immersion high-NA objective (20 $\times$ , NA = 1.0) was raster scanned next to the nanostructured probe submerged in a homogeneously fluorescent solution. The PMTs on the “microscope” and the “fiber” paths simultaneously detected fluorescence light. While the microscope path served as an imaging reference, the fiber path provided information on the structures collection diagrams. The collected light was filtered using bandpass filters (510–560 and 570–640 nm). Images were processed using Fiji by subtracting background noise and applying a moving Gaussian filter over 2 pixels. The collection angles were extracted following the predominant directions on the image.

**Raman Spectroscopy with nTFs:** To acquire Raman spectra with the nTFs, a custom Raman microscope was built. The probe was held, immersed in the analyte, in the focal plane of the microscope, with the back of the taper facing the lens, and 785 nm laser light, filtered with a laser line filter (785  $\pm$  12.5 nm) was injected over the full angular acceptance of the fibers (typically, 0.22 NA). When the probe was immersed in oil, the Raman signal was discriminated using a dichroic

mirror and a long pass razor-edge filter. The spectra were detected using a Horiba iHR320 spectrometer with a 600 lp mm grating.

**Ray Tracing of Light Propagation in Tapered Optical Fibers:** The angle at which light guided in the tapered portion of the nTF impinges on the curved nanograting depending on their position was simulated by a ray-tracing method (Zemax). Details on the application of ray tracing to simulate optical propagation in tapered optical fibers were reported in previous works.<sup>[39]</sup> Briefly, the propagation of a coherent source light covering the whole fiber NA in the tapered section was simulated. To measure the angle formed with the curved nanograting normal, a detector stack was placed where the taper radius matched the cNG's radius of curvature. The numerical estimation was then confirmed experimentally by measuring the angular intensity profile of 785 nm light emitted from a smooth optical window, opened at the same diameter.

**Theoretical Modeling of Curved Nanostructures:** The curved structures were modeled using a 3D FDTD) model using commercial software (FullWAVE by RSoft). The tapered fiber was assumed to be locally cylindrical.<sup>[33]</sup> In fact, considering a taper angle of 4 $^\circ$  and a nanograting longitudinal side of  $t = 25$   $\mu\text{m}$ , the diameter change  $\Delta d$  along the width of one nanograting is, approximately  $\Delta d = \tan(2^\circ) \cdot L = 0.8$   $\mu\text{m}$ . So for  $\lambda = 785$  nm,  $\Delta d \approx \lambda$ .

The refractive index of glass is taken as 1.45. For gold, a Drude–Lorentz model was used given by the following equation

$$\epsilon_m(\omega) = \epsilon_\infty - \frac{\omega_p^2}{\omega^2 + j\omega\gamma_D} - \sum_{k=1}^{k=1} \frac{\delta_k \omega_k^2}{\omega^2 - \omega_k^2 + 2j\omega\gamma_k} \quad (5)$$

where  $\epsilon_\infty$  is the metal dielectric constant at the high-frequency regime in the Drude model,  $\omega_p$  and  $\gamma_D$  are the plasma and collisions frequencies of free electron gas related to the Drude model, whereas  $\delta_k$ ,  $\omega_k$ , and  $\gamma_k$ ,  $i = 1, 2$  are amplitude, resonant angular frequency and damping constant of each Lorentz-like oscillator, respectively. As described in the main text, the model supported the simulation of nonlinear interactions through the dispersive third-order ( $\chi^3$ ) nonlinear properties.

## Supporting Information

Supporting Information is available from the Wiley Online Library or from the author.

## Acknowledgements

M.D.V., M.G., and Fe.P. jointly supervised and are co-last authors in this work. Fi.P., A.B., and Fe.P. acknowledge funding from the European Research Council under the European Union's Horizon 2020 Research and Innovation Program under Grant Agreement No. 677683. F.D.A., L.M.d.I.P., M.V., M.D.V., and Fe.P. acknowledge funding from the European Union's Horizon 2020 Research and Innovation Program under Grant Agreement No. 828972. Fi.P., M.D.V., and Fe.P. acknowledge that this project has received funding from the European Union's Horizon 2020 Research and Innovation Program under Grant Agreement No. 101016787. M.P., Fe.P., and M.D.V. were funded by the U.S. National Institutes of Health (Grant No. 1UF1NS108177-01).

Open access funding provided by Istituto Italiano di Tecnologia within the CRUI-CARE agreement.

## Conflict of Interest

M.D.V. and Fe.P. are founders and hold private equity in Optogenix, a company that develops, produces, and sells technologies to deliver light into the brain. Fi.P. and M.P. have been employed by Optogenix, a company that develops, produces, and sells technologies to deliver light into the brain.

## Data Availability Statement

The data that support the findings of this study are available from the corresponding author upon reasonable request.

## Keywords

brain implants, optical neural interfaces, optogenetics, plasmonics, tapered optical fibers

Received: August 9, 2021

Revised: October 18, 2021

Published online: December 6, 2021

- [1] M. Häusser, *Nat. Methods* **2014**, *11*, 1012.
- [2] A. M. Aravanis, L.-P. Wang, F. Zhang, L. A. Meltzer, M. Z. Mogri, M. B. Schneider, K. Deisseroth, *J. Neural Eng.* **2007**, *4*, S143.
- [3] H. Adelsberger, O. Garaschuk, A. Konnerth, *Nat. Neurosci.* **2005**, *8*, 988.
- [4] A. N. Zorzos, J. Scholvin, E. S. Boyden, C. G. Fonstad, *Opt. Lett.* **2012**, *37*, 4841.
- [5] R. Scharf, T. Tsunematsu, N. Mcalinden, M. D. Dawson, S. Sakata, K. Mathieson, *Sci. Rep.* **2016**, *6*, 28381.
- [6] N. McAlinden, E. Gu, M. D. Dawson, S. Sakata, K. Mathieson, *Front. Neural Circuits* **2015**, *9*, 25.
- [7] F. Wu, E. Stark, P.-C. Ku, K. D. Wise, G. Buzsáki, E. Yoon, *Neuron* **2015**, *88*, 1136.
- [8] C. Goßler, C. Bierbrauer, R. Moser, M. Kunzer, K. Holc, W. Pletschen, K. Köhler, J. Wagner, M. Schwaerzle, P. Ruther, O. Paul, J. Neef, D. Keppeler, G. Hoch, T. Moser, U. T. Schwarz, *J. Phys. D: Appl. Phys.* **2014**, *47*, 20 5401.
- [9] T.-I. Kim, J. G. Mccall, Y. H. Jung, X. Huang, E. R. Siuda, Y. Li, J. Song, Y. M. Song, H. A. Pao, R.-H. Kim, C. Lu, S. D. Lee, I.-S. Song, G. Shin, R. Al-Hasani, S. Kim, M. P. Tan, Y. Huang, F. G. Omenetto, J. A. Rogers, M. R. Bruchas, *Science* **2013**, *340*, 211.
- [10] A. Mohanty, Q. Li, M. A. Tadayon, S. P. Roberts, G. R. Bhatt, E. Shim, X. Ji, J. Cardenas, S. A. Miller, A. Kepecs, M. Lipson, *Nat. Biomed. Eng.* **2020**, *4*, 223.
- [11] E. Segev, J. Reimer, L. C. Moreaux, T. M. Fowler, D. Chi, W. D. Sacher, M. Lo, K. Deisseroth, A. S. Tolias, A. Faraon, M. L. Roukes, *Neurophotonics* **2016**, *4*, 011002.
- [12] F. Pisanello, G. Mandelbaum, M. Pisanello, I. A. Oldenburg, L. Sileo, J. E. Markowitz, R. E. Peterson, A. Della Patria, T. M. Haynes, M. S. Emara, B. Spagnolo, S. R. Datta, M. De Vittorio, B. L. Sabatini, *Nat. Neurosci.* **2017**, *20*, 1180.
- [13] S. Vasudevan, J. Kajtez, A.-I. Bunea, A. Gonzalez-Ramos, T. Ramos-Moreno, A. Heiskanen, M. Kokaia, N. B. Larsen, A. Martínez-Serrano, S. S. Keller, J. Emnéus, *Adv. Sci.* **2019**, *6*, 1902011.
- [14] S. Park, Y. Guo, X. Jia, H. K. Choe, B. Grena, J. Kang, J. Park, C. Lu, A. Canales, R. Chen, Y. S. Yim, G. B. Choi, Y. Fink, P. Anikeeva, *Nat. Neurosci.* **2017**, *20*, 612.
- [15] L. Lu, P. Gutruf, L. Xia, D. L. Bhatti, X. Wang, A. Vazquez-Guardado, X. Ning, X. Shen, T. Sang, R. Ma, G. Pakeltis, G. Sobczak, H. Zhang, D.-O. Seo, M. Xue, L. Yin, D. Chanda, X. Sheng, M. R. Bruchas, J. A. Rogers, *Proc. Natl. Acad. Sci. USA* **2018**, *115*, E1374.
- [16] E. Iseri, D. Kuzum, *J. Neural Eng.* **2017**, *14*, 031001.
- [17] L. C. Moreaux, D. Yatsenko, W. D. Sacher, J. Choi, C. Lee, N. J. Kubat, R. J. Cotton, E. S. Boyden, M. Z. Lin, L. Tian, A. S. Tolias, J. K. S. Poon, K. L. Shepard, M. L. Roukes, *Neuron* **2020**, *108*, 66.
- [18] J. L. Carvalho-De-Souza, J. S. Treger, B. Dang, S. B. H. Kent, D. R. Pepperberg, F. Bezanilla, *Neuron* **2015**, *86*, 207.
- [19] C. Paviolo, J. W. Haycock, P. J. Cadusch, S. L. McArthur, P. R. Stoddart, *J. Biophotonics* **2014**, *7*, 761.
- [20] M. G. Shapiro, K. Homma, S. Villarreal, C.-P. Richter, F. Bezanilla, *Nat. Commun.* **2012**, *3*, 736.
- [21] J. L. Carvalho-De-Souza, B. I. Pinto, D. R. Pepperberg, F. Bezanilla, *Biophys. J.* **2018**, *114*, 283.
- [22] S. Ae Kim, K. M. Byun, J. Lee, J. H. Kim, D.-G. Albert Kim, H. Baac, M. L. Shuler, S. J. Kim, *Opt. Lett.* **2008**, *33*, 914.
- [23] C. L. Howe, K. F. Webb, S. A. Abayezed, D. J. Anderson, C. Denning, N. A. Russell, *J. Phys. D: Appl. Phys.* **2019**, *52*, 104001.
- [24] J. Zhang, T. Atay, A. V. Nurmikko, *Nano Lett.* **2009**, *9*, 519.
- [25] A. Habib, X. Zhu, U. I. Can, M. L. Mclanahan, P. Zorlutuna, A. A. Yanik, *Sci. Adv.* **2019**, *5*, eaav9786.
- [26] F. De Angelis, M. Malerba, M. Patrini, E. Miele, G. Das, A. Toma, R. P. Zaccaria, E. Di Fabrizio, *Nano Lett.* **2013**, *13*, 3553.
- [27] M. Dipalo, G. C. Messina, H. Amin, R. La Rocca, V. Shalabaeva, A. Simi, A. Maccione, P. Zilio, L. Berdondini, F. De Angelis, *Nanoscale* **2015**, *7*, 3703.
- [28] K. Eom, J. Kim, J. M. Choi, T. Kang, J. W. Chang, K. M. Byun, S. B. Jun, S. J. Kim, *Small* **2014**, *10*, 3853.
- [29] T. W. Ebbesen, H. J. Lezec, H. F. Ghaemi, T. Thio, P. A. Wolff, *Nature* **1998**, *391*, 667.
- [30] R. Gordon, D. Sinton, K. L. Kavanagh, A. G. Brolo, *Acc. Chem. Res.* **2008**, *41*, 1049.
- [31] Y. C. Jun, K. C. Y. Huang, M. L. Brongersma, *Nat. Commun.* **2011**, *2*, 283.
- [32] G. Lozano, D. J. Louwers, S. R. Rodríguez, S. Murai, O. T. Jansen, M. A. Verschuuren, J. Gómez Rivas, *Light: Sci. Appl.* **2013**, *2*, e66.
- [33] A. W. Snyder, J. D. Love, *Optical Waveguide Theory* (Ed: D. John), Chapman and Hall, London **1983**.
- [34] M. Pisanello, F. Pisano, L. Sileo, E. Maglie, E. Bellistri, B. Spagnolo, G. Mandelbaum, B. L. Sabatini, M. De Vittorio, F. Pisanello, *Sci. Rep.* **2018**, *8*, 4467.
- [35] H. F. Ghaemi, T. Thio, D. E. Grupp, T. W. Ebbesen, H. J. Lezec, *Phys. Rev. B: Condens. Matter Mater. Phys.* **1998**, *58*, 6779.
- [36] F. Pisano, A. Balena, M. F. Kashif, M. Pisanello, G. De Marzo, L. Algieri, A. Quattieri, L. Sileo, T. Stomeo, A. D'orazio, M. De Vittorio, F. Pisanello, M. Grande, *Nanotechnology* **2020**, *31*, 435301.
- [37] J. A. Kurvits, M. Jiang, R. Zia, *J. Opt. Soc. Am. A* **2015**, *32*, 2082.
- [38] S. A. Maier, *Plasmonics: Fundamentals and Applications*, Springer, Berlin **2007**.
- [39] E. Maglie, M. Pisanello, F. Pisano, A. Balena, M. Bianco, B. Spagnolo, L. Sileo, B. L. Sabatini, M. De Vittorio, F. Pisanello, *Opt. Lett.* **2020**, *45*, 3856.
- [40] A. Balena, M. Bianco, F. Pisano, M. Pisanello, L. Sileo, B. L. Sabatini, M. D. Vittorio, F. Pisanello, *Opt. Express* **2020**, *28*, 21368.
- [41] A. Foti, C. D'andrea, F. Bonaccorso, M. Lanza, G. Calogero, E. Messina, O. M. Maragò, B. Fazio, P. G. Gucciardi, *Plasmonics* **2013**, *8*, 13.
- [42] F. Pisano, M. Pisanello, S. J. Lee, J. Lee, E. Maglie, A. Balena, L. Sileo, B. Spagnolo, M. Bianco, M. Hyun, M. De Vittorio, B. L. Sabatini, F. Pisanello, *Nat. Methods* **2019**, *16*, 1185.
- [43] M. Jermyn, K. Mok, J. Mercier, J. Desroches, J. Pichette, K. Saint-Arnaud, L. Bernstein, M.-C. Guiot, K. Petrecca, F. Leblond, *Sci. Transl. Med.* **2015**, *7*, 274ra19.
- [44] X.-F. Zhang, M.-Q. Zou, X.-H. Qi, F. Liu, C. Zhang, F. Yin, *J. Raman Spectrosc.* **2011**, *42*, 1784.
- [45] K. Czamara, K. Majzner, M. Z. Pacia, K. Kochan, A. Kaczor, M. Baranska, *J. Raman Spectrosc.* **2015**, *46*, 4.
- [46] W. C. Zúñiga, V. Jones, S. M. Anderson, A. Echevarria, N. L. Miller, C. Stashko, D. Schmolze, P. D. Cha, R. Kothari, Y. Fong, M. C. Storrie-Lombardi, *Sci. Rep.* **2019**, *9*, 14639.

- [47] D. Débarre, W. Supatto, A.-M. Pena, A. Fabre, T. Tordjmann, L. Combettes, M.-C. Schanne-Klein, E. Beaufort, *Nat. Methods* **2006**, 3, 47.
- [48] R. W. Boyd, *Nonlinear Optics*, Academic Press, San Diego, CA **2020**.
- [49] D. Harris-Birtill, M. Singh, Y. Zhou, A. Shah, P. Ruenraroengsak, M. E. Gallina, G. B. Hanna, A. E. G. Cass, A. E. Porter, J. Bamber, D. S. Elson, *PLoS One* **2017**, 12, e0185990.
- [50] E. Giorgetti, M. Muniz-Miranda, P. Marsili, D. Scarpellini, F. Giammanco, *J. Nanopart. Res.* **2012**, 14, 648.
- [51] J. Zhang, M. Irannejad, B. Cui, *Plasmonics* **2015**, 10, 831.
- [52] W. D. Sacher, F.-D. Chen, H. Moradi-Chameh, X. Luo, A. Fomenko, P. T. Shah, T. Lordello, X. Liu, I. F. Almog, J. N. Straguzzi, T. M. Fowler, Y. Jung, T. Hu, J. Jeong, A. M. Lozano, P. G.-Q. Lo, T. A. Valiante, L. C. Moreaux, J. K. S. Poon, M. L. Roukes, *Neurophotonics* **2021**, 8, 025003.
- [53] A. Tuniz, M. A. Schmidt, *Nanophotonics* **2018**, 7, 1279.
- [54] J. Cao, D. Zhao, Q. Mao, *Analyst* **2017**, 142, 596.
- [55] Z. Chen, Z. Dai, N. Chen, S. Liu, F. Pang, B. Lu, T. Wang, *IEEE Photonics Technol. Lett.* **2014**, 26, 777.
- [56] J. Zhang, S. Chen, T. Gong, X. Zhang, Y. Zhu, *Plasmonics* **2016**, 11, 743.
- [57] J. Cao, D. Zhao, Y. Qin, *Talanta* **2019**, 194, 895.
- [58] C. Wang, L. Zeng, Z. Li, D. Li, *J. Raman Spectrosc.* **2017**, 48, 1040.
- [59] C. Ropers, C. C. Neacsu, T. Elsaesser, M. Albrecht, M. B. Raschke, C. Lienau, *Nano Lett.* **2007**, 7, 2784.
- [60] F. Lu, W. Zhang, L. Huang, S. Liang, D. Mao, F. Gao, T. Mei, J. Zhao, *Opto-Electron. Adv.* **2018**, 1, 18001001.
- [61] T. Umakoshi, Y. Saito, P. Verma, *Nanoscale* **2016**, 8, 5634.
- [62] S. Li, S. Yang, *J. Phys. D: Appl. Phys.* **2020**, 53, 8.
- [63] M. Horák, K. Bukvišová, V. Švarc, J. Jaskowiec, V. Krápek, T. Šíkola, *Sci. Rep.* **2018**, 8, 9640.
- [64] A. Khaleque, E. G. Mironov, J. H. Osório, Z. Li, C. M. B. Cordeiro, L. Liu, M. A. R. Franco, J.-L. Liow, H. T. Hattori, *Opt. Express* **2017**, 25, 8986.
- [65] E. J. Smythe, M. D. Dickey, J. Bao, G. M. Whitesides, F. Capasso, *Nano Lett.* **2009**, 9, 1132.
- [66] Y. Fu, N. K. A. Bryan, *Appl. Phys. B* **2005**, 80, 581.
- [67] J. A. Kim, D. J. Wales, A. J. Thompson, G.-Z. Yang, *Adv. Opt. Mater.* **2020**, 8, 1901934.
- [68] D. Franklin, Z. He, P. Mastranzo Ortega, A. Safaei, P. Cencillo-Abad, S.-T. Wu, D. Chanda, *Proc. Natl. Acad. Sci. USA* **2020**, 117, 13350.
- [69] L. Li, Y. Liang, X. Zong, Y. Liu, *Opt. Express* **2020**, 28, 695.
- [70] S. Aksu, M. Huang, A. Artar, A. A. Yanik, S. Selvarasah, M. R. Dokmeci, H. Altug, *Adv. Mater.* **2011**, 23, 4422.
- [71] P. Pai, J. Bosch, M. Kühmayer, S. Rotter, A. P. Mosk, *Nat. Photonics* **2021**, 15, 431.
- [72] D. E. Boonzajer Flaes, J. Stopka, S. Turtaev, J. F. De Boer, T. Tyc, T. Čížmár, *Phys. Rev. Lett.* **2018**, 120, 233901.
- [73] Z. Li, X. Tian, C.-W. Qiu, J. S. Ho, *Nat. Electron.* **2021**, 4, 382.
- [74] M. L. Tseng, Y. Jahani, A. Leitis, H. Altug, *ACS Photonics* **2020**, 8, 47.
- [75] L. Sileo, M. Pisanello, M. De Vittorio, F. Pisanello, *Proc. SPIE* **2015**, 9305, 93052O.
- [76] S. Preibisch, S. Saalfeld, P. Tomancak, *Bioinformatics* **2009**, 25, 1463.
- [77] M. Pisanello, F. Pisano, M. Hyun, E. Maglie, A. Balena, M. De Vittorio, B. L. Sabatini, F. Pisanello, *Front. Neurosci.* **2019**, 13, 82.
- [78] M. Bianco, A. Balena, M. Pisanello, F. Pisano, L. Sileo, B. Spagnolo, C. Montinaro, B. L. Sabatini, M. D. Vittorio, F. Pisanello, *Biomed. Opt. Express* **2021**, 12, 993.